

# Structural and electrical properties of $\text{Ba}(\text{Sb}_{1/2}\text{Nb}_{1/2})\text{O}_3$ ceramic

K. Prasad · K. P. Chandra · Priyanka ·  
A. R. Kulkarni

Received: 19 July 2010/Accepted: 29 October 2010/Published online: 11 November 2010  
© Springer Science+Business Media, LLC 2010

**Abstract** Lead-free perovskite  $\text{Ba}(\text{Sb}_{1/2}\text{Nb}_{1/2})\text{O}_3$  was prepared by conventional ceramic fabrication technique at 1200 °C/5 h in air atmosphere. The crystal symmetry, space group and unit cell dimensions were determined from the experimental results using FullProf software whereas crystallite size and lattice strain were estimated from Williamson–Hall approach. XRD analysis of the compound indicated the formation of a single-phase monoclinic structure with the space group  $P2/m$ . EDAX and SEM studies were carried out to evaluate the quality and purity of the compound. Dielectric study revealed the frequency-dependent dielectric anomaly. To find a correlation between the response of the real system and idealized model circuit composed of discrete electrical components, the model fittings were presented using the impedance data. Complex impedance analyses suggested the dielectric relaxation to be of non-Debye type. The correlated barrier hopping model was employed to successfully explain the mechanism of charge transport in  $\text{Ba}(\text{Sb}_{1/2}\text{Nb}_{1/2})\text{O}_3$ . The ac conductivity data were used to evaluate the density of states at Fermi level, minimum hopping length and apparent activation energy of the compound.

## Introduction

Development of perovskite  $\text{ABO}_3$ -type materials exhibiting high dielectric constant are of considerable interest nowadays as they play an important role in electronics/microelectronics and have various technological applications. It has been observed that most of the high dielectric constant materials contain lead which inevitably causes environmental pollution due to the toxicity of lead oxide. It is, therefore, necessary to search alternative lead-free compounds for such applications, which should have either comparable or superior dielectric properties. Also, it is observed that modification at B-site plays an important role in tailoring the properties of  $\text{A}(\text{B}'\text{B}'')\text{O}_3$  complex perovskites as the material's properties depend mainly on the size difference of pseudo-cation  $(\text{B}'\text{B}'')^{4+}$  and on the difference on their valance states. During the past few years, several investigations have been carried to study the electrical properties of  $\text{Ba}(\text{Fe}_{1/2}\text{Nb}_{1/2})\text{O}_3$  [1–6],  $\text{Ba}(\text{Al}_{1/2}\text{Nb}_{1/2})\text{O}_3$  [7, 8],  $\text{Ba}(\text{Bi}_{1/2}\text{Nb}_{1/2})\text{O}_3$  [9, 10],  $\text{Ba}(\text{In}_{1/2}\text{Nb}_{1/2})\text{O}_3$  [11],  $\text{Ba}(\text{Ni}_{1/2}\text{Nb}_{1/2})\text{O}_3$  [12],  $\text{Sr}(\text{Fe}_{1/2}\text{Nb}_{1/2})\text{O}_3$  [3],  $\text{Ba}(\text{Y}_{1/2}\text{Nb}_{1/2})\text{O}_3$  [13],  $\text{Ba}(\text{La}_{1/2}\text{Nb}_{1/2})\text{O}_3$  [14],  $\text{Ba}(\text{Fe}_{1/2}\text{Ta}_{1/2})\text{O}_3$  [15], etc. for their possible applications in electronic and/or micro-electronic devices. They are mechanically tough and show excellent dielectric properties. Besides, recent works on the A-site-modified perovskite compounds such as  $(\text{Na}_{1/2}\text{Bi}_{1/2})\text{TiO}_3$  and  $(\text{Na}_{1/2}\text{Sb}_{1/2})\text{TiO}_3$  also showed excellent electrical properties [16, 17]. Therefore, it will be interesting to see the effect of B-site modification on the structural and electrical properties of one such ceramic  $\text{Ba}(\text{Sb}_{1/2}\text{Nb}_{1/2})\text{O}_3$ .

An extensive literature survey suggested that no attempt, to the authors' knowledge, has so far been made to study perovskite  $\text{Ba}(\text{Sb}_{1/2}\text{Nb}_{1/2})\text{O}_3$ . The material is mechanically tough and lead-free. Accordingly, in this

K. Prasad (✉) · Priyanka  
Materials Research Laboratory, University Department of  
Physics, T.M. Bhagalpur University, Bhagalpur 812 007, India  
e-mail: k.prasad65@gmail.com; k\_prasad65@yahoo.co.in

K. P. Chandra  
Department of Physics, S.M. College, Bhagalpur 812 001, India

A. R. Kulkarni  
Department of Metallurgical Engineering and Materials Science,  
Indian Institute of Technology, Mumbai 400 076, India

study, the structural, microstructural, dielectric, impedance and ac electrical conductivity studies on Ba(Sb<sub>1/2</sub>Nb<sub>1/2</sub>)O<sub>3</sub> ceramic have been presented. Also, an attempt has been made to explain the conduction mechanism in Ba(Sb<sub>1/2</sub>Nb<sub>1/2</sub>)O<sub>3</sub>.

## Experimental

Polycrystalline Ba(Sb<sub>1/2</sub>Nb<sub>1/2</sub>)O<sub>3</sub> (abbreviated hereafter as BSN) was prepared from AR grade chemicals (Merck, 99.99%): BaCO<sub>3</sub>, Sb<sub>2</sub>O<sub>3</sub> and Nb<sub>2</sub>O<sub>5</sub> using solid-state synthesis according to the thermo-chemical reaction: BaCO<sub>3</sub> +  $\frac{1}{4}$ Sb<sub>2</sub>O<sub>3</sub> +  $\frac{1}{4}$ Nb<sub>2</sub>O<sub>5</sub>  $\xrightarrow{\Delta}$  Ba(Sb<sub>1/2</sub>Nb<sub>1/2</sub>)O<sub>3</sub> + ↑ CO<sub>2</sub>(g) at 1200 °C for 5 h under a controlled heating and cooling cycles. Circular disc-shaped pellets were made by applying uniaxial pressure of about 650 MPa. The pellet was subsequently sintered at 1250 °C under air atmosphere for 4 h. The completion of reaction and the formation of desired compound were checked by X-ray diffraction technique. The weight of the compound (powder) was monitored before and after sintering. The maximum difference was about 1.93 mg for the total of 10 g of the powder. Therefore, the composition of the sample was considered to be the same as initial.

The XRD spectra were taken on sintered pellet of BSN with an X-ray diffractometer (XPERT-PRO, Pan Analytical) at room temperature, using CuK $\alpha$  radiation ( $\lambda = 1.5405 \text{ \AA}$ ), between the Bragg angles 20° to 85° with a scanning speed of 5.08° min<sup>-1</sup>. The XY (2θ vs. intensity) data obtained from this experiment were plotted with the WinPLOTR program, and the angular positions of the peaks were obtained with the same program [18]. The dimensions of the unit cell, *hkl* values and space group of BSN were obtained using the TREOR program in the FullProf 2000 software package and then refinement was carried out through the profile matching routine of FullProf [19]. The Bragg peaks were modelled with pseudo-Voigt function, and the background was estimated by linear interpolation between selected background points. The SEM and EDAX of the sintered BSN sample were taken on the fractured surface using a computer-controlled scanning electron microscope (SEM Hitachi S-3400 N, Japan). Real and imaginary parts of the electrical impedance were measured as functions of frequency (1 Hz–1 MHz) and temperature (50–450 °C) using a computer-controlled Solartron SI1260 impedance/gain-phase analyser in a cooling mode on a symmetrical cell of type Ag|BSN|Ag, where Ag is a conductive paint coated on either side of the pellet. The temperature was varied at a rate of 1 °C/min.

## Theoretical background

The real and imaginary parts of dielectric constant were obtained from the impedance data in a conventional way using the following relations [8]:

$$\epsilon'(\omega) = Z''/\omega C_0 |Z|^2 \quad (1)$$

$$\epsilon''(\omega) = Z'/\omega C_0 |Z|^2 \quad (2)$$

where  $|Z| = [(Z')^2 + (Z'')^2]^{1/2}$  and  $\omega (= 2\pi f)$  is the angular frequency and  $f$  is the operating frequency. The ac conductivity data were obtained using a relation  $\sigma^*(\omega) = \sigma'(\omega) + i\sigma''(\omega) = i\omega\epsilon_0\epsilon^*(\omega)$  and the real and imaginary part of  $\sigma^*(\omega)$  were obtained as:

$$\sigma'(\omega) = \omega\epsilon_0\epsilon''(\omega) \quad (3)$$

$$\sigma''(\omega) = \omega\epsilon_0\epsilon'(\omega) \quad (4)$$

In the conductivity representation for electronic conduction, the real part  $\sigma'(\omega)$  should be constant and imaginary part  $\sigma''$  increases linearly with frequency. The ac electrical conductivity in most of the materials due to localized states is given by:

$$\sigma'(\omega) = \sigma_0 + A\omega^s \quad (5)$$

where  $\sigma_0$  is the frequency-independent (electronic or dc) part of ac conductivity,  $s$  ( $0 \leq s \leq 1$ ) is the index,  $\omega$  is angular frequency of applied ac field and  $A [= \pi N^2 e^2 / 6k_B T (2\alpha)]$  is a constant,  $e$  is the electronic charge,  $T$  is the temperature,  $\alpha$  is the polarizability of a pair of sites and  $N$  is the number of sites per unit volume amongst which hopping takes place. Such variation is associated with displacement of carriers which move within the sample by discrete hops of length  $R$  between randomly distributed localized sites. The term  $A\omega^s$  can often be explained on the basis of two distinct mechanisms for carrier conduction: (i) quantum mechanical tunnelling through the barrier separating the localized sites and (ii) correlated barrier hopping (CBH) over the same barrier. In these models, the exponent  $s$  is found to have two different trends of variation with temperature and frequency. Further, if ac conductivity supports CBH [20],

$$\sigma' = \frac{\pi}{3} e^2 \omega k_B T [N(E_f)]^2 \alpha^{-5} [\ln(f_0/\omega)]^4 \quad (6)$$

where  $N(E_f)$  is the density of states at Fermi level,  $f_0$  the photon frequency and  $\alpha$  is the localized wave function. The exponent  $s$  and minimum hopping length,  $R_{\min}$  can be expressed as [21, 22]:

$$s = 1 - (6k_B T / W_m) \quad (7)$$

$$R_{\min} = 2e^2 / \pi\epsilon\epsilon_0 W_m \quad (8)$$

where  $W_m$  is the binding energy, which is defined as the energy required to remove an electron completely from one site to the another site.

## Results and discussion

### Structural and microstructural studies

Rietveld refinements on the X-ray (XRD) data were done on BSN, selecting the space group  $P2/m$ . Figure 1 depicts the observed, calculated and difference XRD profiles for BSN after the final cycle of refinement. It can be seen that the profiles for observed and calculated one are perfectly matching. The value of  $\chi^2$  comes out to be 8.835, which may be considered to be very good for estimations. The profile fitting procedure adopted was minimizing the  $\chi^2$  function [23]. The XRD analyses indicated that BSN has a monoclinic unit cell. The crystal data and refinement factors of  $\text{Ba}(\text{Sb}_{1/2}\text{Nb}_{1/2})\text{O}_3$  obtained from XRD data are depicted in Table 1.

Figure 2 shows the SEM-micrograph and EDAX pattern of fractured surface of sintered BSN. All the peaks in the EDAX pattern have perfectly assigned to the elements present in  $\text{Ba}(\text{Sb}_{1/2}\text{Nb}_{1/2})\text{O}_3$ . This clearly indicated the purity of chemical composition of BSN. The well-organized grains of unequal sizes ( $\sim 5\text{--}8 \mu\text{m}$ ) appear to be distributed throughout the sample in the SEM-micrograph.

### Dielectric studies

The frequency dependence  $\epsilon'$  and  $\epsilon''$  at different temperatures have been plotted in Fig. 3. It is observed that both  $\epsilon'$  and  $\epsilon''$  follow inverse dependence on frequency. Dispersion with relatively high dielectric constant can be seen in the  $\epsilon' - f$  graph in the lower frequency region and the dielectric constant drops at high frequencies. A relatively high dielectric constant at low frequencies is a characteristic of a dielectric material. This may be due to the space charge contribution. At very low frequencies, dipoles follow the field and we have  $\epsilon' \approx \epsilon_s$  (value of dielectric constant at quasi static fields). As the frequency increases

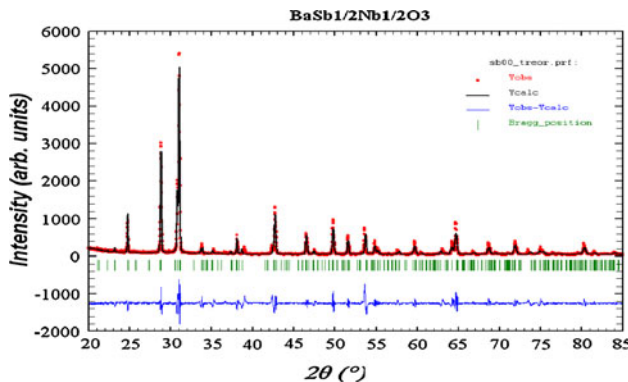


**Fig. 1** Rietveld refined pattern of sintered  $\text{Ba}(\text{Sb}_{1/2}\text{Nb}_{1/2})\text{O}_3$  in the space group  $P2/m$ . Symbols represent the observed data points and the solid lines their Rietveld fit

dipoles begin to lag behind the field and  $\epsilon'$  slightly decreases. When frequency reaches the characteristic frequency, the dielectric constant drops (relaxation process) and at very high frequencies, dipoles can no longer follow the field and  $\epsilon' \approx \epsilon_\infty$ .

Figure 4 illustrates the temperature dependence of  $\epsilon'$  and  $\epsilon''$  of BSN at different frequencies. It is found that both  $\epsilon'$  and  $\epsilon''$  first decrease and then start increasing with the rise in temperature and ultimately find a maximum for all the frequencies. Also, the peaks in  $\epsilon'$  shift to higher temperatures (from 431 °C at 1 Hz to 441 °C at 10 kHz) upon increasing frequency. This indicates the relaxor-like behaviour of BSN. The values of  $\epsilon'$  and  $\epsilon''$  at room temperature are, respectively, found to be 37.5 and 48.8 at 1 kHz.

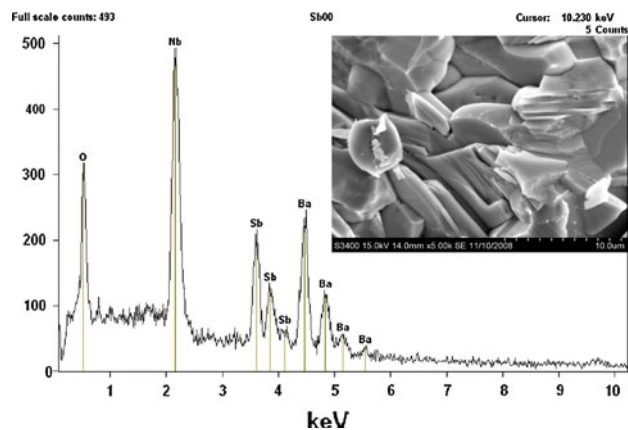
### Impedance studies

Figure 5 shows the variation of  $Z'$  and  $Z''$  with frequency at different temperatures. It is observed that the magnitude of  $Z'$  decreases with the increase of frequency for all the temperatures which indicates an increase in ac conductivity with the rise in frequency. Further, at low frequencies the  $Z'$  values flatten with rise in temperature. The values of  $Z''$  reach a maximum peak ( $Z''_{\max}$ ) which are slightly asymmetric in nature. Also, the values of  $Z''_{\max}$  first increase to 150 °C which shift towards lower frequency side afterwards it decreases and shift towards higher frequency side with increasing temperature. The asymmetric broadening of peaks in  $Z'' - f$  plots suggests that there is a spread of relaxation times, thereby indicating the existence of a temperature-dependent electrical relaxation in the material [24].

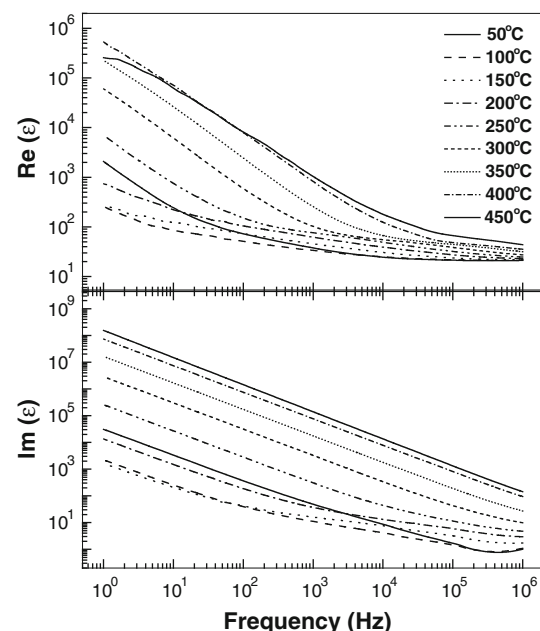
Figure 6 shows the complex impedance spectrum at two representative temperatures along with the fitted data. Complex impedance plots do not always yield perfect or depressed semicircular arcs, and often the arc is asymmetric and cannot be well approximated by the combinations of impedances and capacitances only. The appropriate equivalent circuit at each temperature is illustrated in the insets of Fig. 6. It can be seen that a constant phase element (CPE) is connected throughout the temperature range of measurement whilst a Warburg element ( $W$ ) is connected at 200 °C. The parameters of each fitting are shown in the respective circuit and were determined using a non-linear least-square fitting algorithm [25]. The admittance of CPE and Warburg admittance were estimated using the relations:  $Y_0 = Q(j\omega)^n$ , and  $Y_W(\omega) = \sqrt{\omega}/[W(1-j)]$ , where  $Q$  is constant pre-factor,  $n$  is exponent and  $j = \sqrt{-1}$  is the imaginary unit. The introduction of CPE in the equivalent circuit may be due to the distribution of reaction rates and/or surface roughness, and the Warburg element may be due

**Table 1** The crystal data and refinement factors of Ba(Sb<sub>1/2</sub>Nb<sub>1/2</sub>)O<sub>3</sub> obtained from X-ray powder diffraction data

Parameters	Results	Description of parameters
Crystal system	Monoclinic	$R_p$ (profile factor) = $100[\sum y_i - y_{ic} /\sum y_i ]$ , where $y_i$ is the observed intensity and $y_{ic}$ is the calculated intensity at the $i^{\text{th}}$ step.
Space group	$P2/m$	$R_{wp}$ (weighted profile factor) = $100[\sum\omega_i y_i - y_{ic} ^2/\sum\omega_i(y_i)^2]^{1/2}$ , where $\omega_i = 1/\sigma_i^2$ and $\sigma_i^2$ is variance of the observation.
$a$ (Å)	7.8699	$R_{exp}$ (expected weighted profile factor) = $100[(n - p)/\sum\omega_i(y_i)^2]^{1/2}$ , where $n$ and $p$ are the number of profile points and refined parameters, respectively.
$b$ (Å)	6.1865	$R_B$ (Bragg factor) = $100[\sum I_{obs} - I_{calc} /\sum I_{obs} ]$ , where $I_{obs}$ is the observed integrated intensity and $I_{calc}$ is the calculated integrated intensity.
$c$ (Å)	5.9125	$R_F$ (crystallographic $R_F$ factor) = $100[\sum F_{obs} - F_{calc} /\sum F_{obs} ]$ , where $F$ is the structure factor, $F = \sqrt{(I/L)}$ , where $L$ is Lorentz polarization factor.
$\alpha$ (°)	90.000	$\chi^2 = \sum\omega_i(y_i - y_{ic})^2$ .
$\beta$ (°)	103.226	$d$ (Durbin-Watson statistics) = $\sum\{[\omega_i(y_i - y_{ic}) - \omega_{i-1}(y_{i-1} - y_{ic-1})]^2\}/\sum[\omega_i(y_i - y_{ic})]^2$ .
$\gamma$ (°)	90.000	$Q_D$ = expected $d$ .
$V$ (Å <sup>3</sup> )	280.232	$S$ (goodness of fit) = $(R_{wp}/R_{exp})$ .
$R_p$	47.5	
$R_{wp}$	43.6	
$R_{exp}$	14.7	
$R_B$	0.0235	
$R_F$	0.0835	
$\chi^2$	8.835	
$d$	0.3595	
$Q_D$	1.9092	
$S$	2.966	

**Fig. 2** EDAX spectrum and SEM micrograph of fractured surface of Ba(Sb<sub>1/2</sub>Nb<sub>1/2</sub>)O<sub>3</sub> ceramic

to the semi-infinite linear diffusion, i.e. unrestricted diffusion to a large planar electrode, which obeys second Fick's law. Also, all these curves do not coincide with origin (zero value), and hence a series resistance has been introduced that can be ascribed to the LCR circuit representation of the sample [26]. The impedance data did not fit well with single/double RC-combination, rather this fit excellently well ( $\chi^2 \sim 10^{-5}$ ) with  $R(C(R(Q(RW)))(CR)-$  and  $R(C(R(QR)))(CR)$ -type of equivalent circuits at 200 and 400 °C, respectively (insets of Fig. 6), indicating thereby that the electrical responses are due to the grain and grain boundary effects [24, 26]. Here, symbols  $R$ ,  $C$ ,  $Q$  and  $W$  represent

**Fig. 3** Variation of real and imaginary parts of dielectric constant with frequency at different temperatures for Ba(Sb<sub>1/2</sub>Nb<sub>1/2</sub>)O<sub>3</sub> ceramic

resistance, capacitance, constant-phase element and Warburg element, respectively. Further, it is known that for Debye-type relaxation, the centre of the semicircular plots should be located on the  $Z'$ -axis, whereas for a non-Debye type relaxation these Argand plane plots are close to semicircular

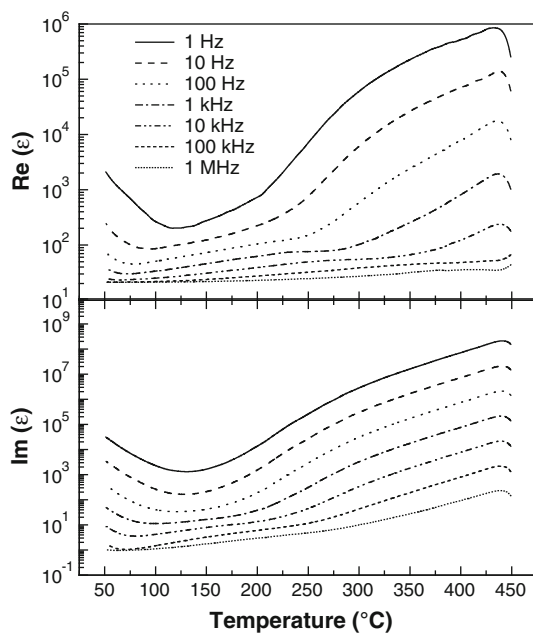


**Fig. 4** Variation of real and imaginary parts of dielectric constant with temperature at different frequencies for  $\text{Ba}(\text{Sb}_{1/2}\text{Nb}_{1/2})\text{O}_3$  ceramic

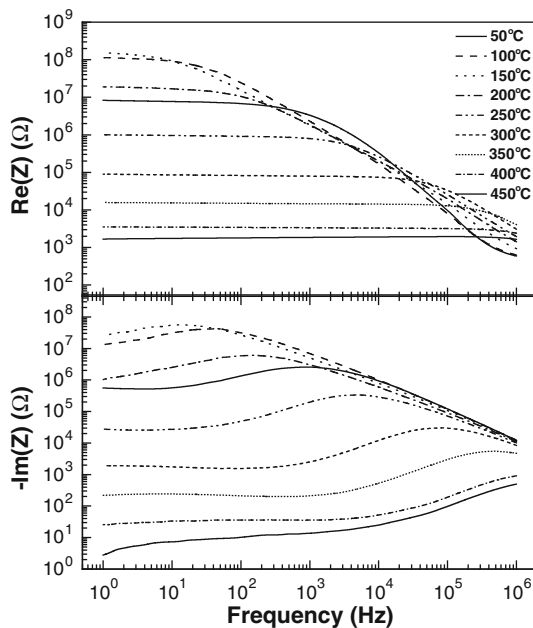


**Fig. 5** Variation of real and imaginary parts of impedance with frequency at different temperatures for  $\text{Ba}(\text{Sb}_{1/2}\text{Nb}_{1/2})\text{O}_3$  ceramic

arcs with end-points on the real axis and the centre lies below this axis. The complex impedance in such a case can be described as:

$$Z^*(\omega) = Z' + iZ'' = R/[1 + (i\omega/\omega_0)^{1-\alpha}] \quad (9)$$

where  $\alpha$  represents the magnitude of the departure of the electrical response from an ideal condition, and this can be

determined from the location of the centre of the semicircles. Also, it is known that when  $\alpha$  approaches zero, i.e.  $\{(1 - \alpha) \rightarrow 1\}$ , Eq. 9 gives rise to classical Debye's formalism. It can be seen from the impedance plots that the data are not represented by full semicircle rather they are depressed one, i.e. centres of semicircles lie little below the abscissa  $Z'$ -axis. Here,  $\alpha > 0$  and it increases with the rise in temperature, suggesting the dielectric relaxation to be of non-Debye type in BSN, similar to  $\text{Ba}(\text{Fe}_{1/2}\text{Nb}_{1/2})\text{O}_3$  [6],  $\text{Ba}(\text{Al}_{1/2}\text{Nb}_{1/2})\text{O}_3$  [8] and  $\text{Ba}(\text{Bi}_{1/2}\text{Nb}_{1/2})\text{O}_3$  [9]. This may happen due to the presence of distributed elements in the material-electrode system.

#### AC conductivity studies

Figure 7 shows the log–log plot of real and imaginary parts of ac electrical conductivity ( $\sigma'$  and  $\sigma''$ ) versus frequency at different temperatures. The plots of  $\sigma'$  show dispersion throughout the chosen frequency range and with the increment in temperature plots get flattened (plateau value). The switchover from the frequency-independent to the frequency-dependent regions shows the onset of the conductivity relaxation, indicating the translation from long-range hopping to the short-range ion motion. The values of the index  $s$  were obtained from the slopes of the  $\sigma' - f$  plots in the low frequency region. The inset of Fig. 7 shows the temperature dependence of  $s$ . It can be seen that the value of  $s$  is always less than 1 and decreases with the rise in temperature. Further, the value of  $s$  approaching to zero at higher temperatures indicates that the dc conductivity dominates at higher temperatures in the low frequency region following Eq. 5. The model based on correlated hopping of electrons over barrier predicts a decrease in the value of the index with the increase in temperature and so this is consistent with the experimental results. Therefore, the conduction in the system may be considered to be due to the short-range translational-type hopping of charge carriers. This indicates that the conduction process is a thermally activated process. The imaginary part of the ac conductivity decreases with decreasing frequency.

Hopping conduction mechanism is generally consistent with the existence of a high density of states in the materials having band gap like that of semiconductor. Due to localization of charge carriers, formation of polarons takes place, and the hopping conduction may occur between the nearest neighbouring sites. Figure 8 shows the variation of  $\ln \sigma'$  versus  $10^3/T$  at different frequencies. The conductivity plots clearly show the negative temperature coefficient of resistance (NTCR) character of BSN. The apparent activation energy for conduction was obtained using the Arrhenius relationship:

**Fig. 6** Complex impedance plots (measured and calculated) of Ba(Sb<sub>1/2</sub>Nb<sub>1/2</sub>)O<sub>3</sub> ceramic at two representative temperatures 200 and 400 °C. The insets show the appropriate equivalent electrical circuits

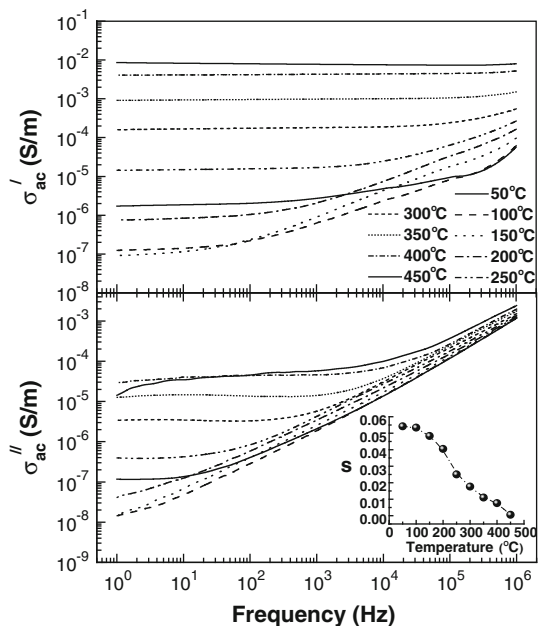
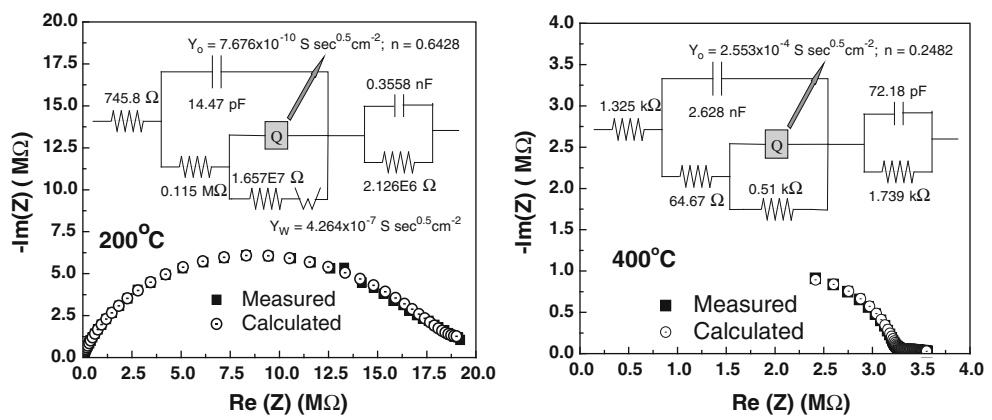


**Fig. 7** Variation of real and imaginary parts of ac conductivity with frequency at different temperatures for Ba(Sb<sub>1/2</sub>Nb<sub>1/2</sub>)O<sub>3</sub> ceramic. Inset: Variation of index  $s$  with temperature

$$\sigma' = \sigma_0 \exp(-E_a/k_B T) \quad (10)$$

A linear least square fitting of the conductivity data to Eq. 10 gives the value of the apparent activation energy,  $E_a$ . The values of  $E_a$  are estimated, respectively, to be 0.47, 0.46 and 0.37 eV at 1 Hz, 1 kHz and 1 MHz. The low value of  $E_a$  may be due to the carrier transport through hopping between localized states in a disordered manner [27]. Inset of Fig. 8 shows the plot of scaled  $Z''$  versus reduced frequency,  $f/f_{max}$ . It can be seen that the scaled data points coalesced into a master curve. The value of full width at half maximum (FWHM) is found to be  $>1.14$  decades. These observations indicate that the distribution function for relaxation times is nearly temperature-independent with non-exponential conductivity relaxation, which suggests the possibility of ion migration that takes

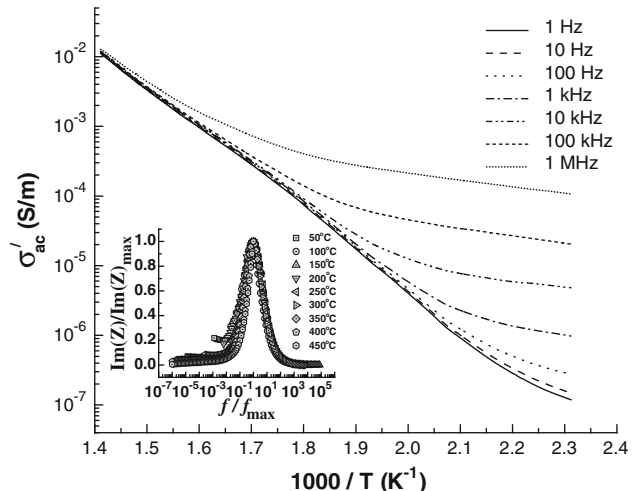


**Fig. 8** Variation of real part of ac conductivity with inverse of temperature at different frequencies for Ba(Sb<sub>1/2</sub>Nb<sub>1/2</sub>)O<sub>3</sub> ceramic. Inset shows the scaling behaviour of  $Im(Z)$

place via hopping accompanied by a consequential time-dependent mobility of other charge carriers of the same type in the vicinity.

The values of  $N(E_f)$  were estimated using Eq. 6 by assuming  $f_0 = 10^{13}$  Hz,  $\alpha = 10^{10}$  m<sup>-1</sup> at various operating frequencies and temperatures. Figure 9 illustrates the frequency dependence of  $N(E_f)$  at different temperatures. It can be seen that the values of  $N(E_f)$  decrease with the increase in the operating frequency and almost merge above 100 kHz. Inset Fig. 9 shows the variation of  $N(E_f)$  with temperature at different frequencies. It is seen that the  $N(E_f)$  increases with the increase in temperature and finds a peak for all the frequencies similar to dielectric measurement. Therefore, at low frequencies the electrical conduction in the system is being affected by both frequency as well as temperature, whereas at higher frequencies the charge carriers are localized and being affected by thermal excitations. The reasonably high values of  $N(E_f)$  suggest that the hopping between the pairs of sites dominates the mechanism of charge transport in BSN.

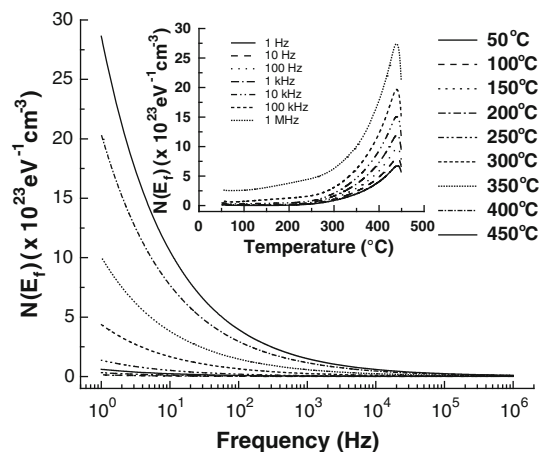


**Fig. 9** Variation of density of states at Fermi level of  $\text{Ba}(\text{Sb}_{1/2}\text{Nb}_{1/2})\text{O}_3$  ceramic with frequency at different temperatures. *Inset:* Temperature dependence of density of states at Fermi level at different frequencies

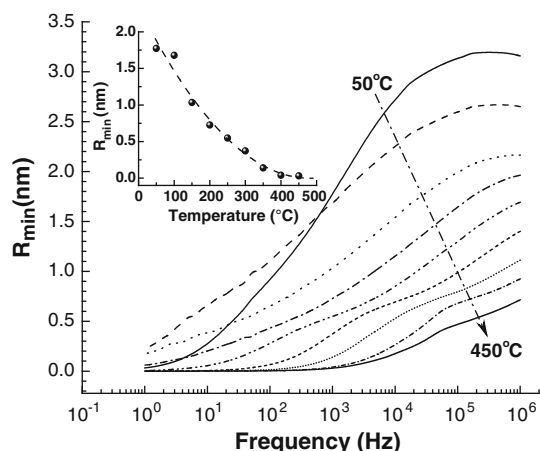


**Fig. 10** Variation of  $R_{\min}$  of  $\text{Ba}(\text{Sb}_{1/2}\text{Nb}_{1/2})\text{O}_3$  ceramic with frequency at different temperatures. *Inset:* Variation of  $R_{\min}$  with temperature at 1 kHz

The value of minimum hopping length,  $R_{\min}$ , was calculated using Eq. 8. Figure 10 presents the variation of  $R_{\min}$  with frequency at different temperatures. It is characterized by very low value ( $\sim 10^{-10}$  m) of  $R_{\min}$  in the lower frequency region, a continuous dispersion with the increase in frequency having a tendency to saturate at a maximum asymptotic value in the higher frequency region. Such observations may possibly be related to a lack of restoring force governing the mobility of charge carriers under the action of an induced electric field [8]. This behaviour supports long-range mobility of charge carriers. Further, a sigmoidal increase in the value of  $R_{\min}$  with the frequency approaching ultimately to a saturation value may be attributed to the conduction phenomenon due to short-range mobility of charge carriers. Inset of Fig. 10 shows the variation of  $R_{\min}$  with temperature at 1 kHz. It can be

seen that the values of  $R_{\min}$  decrease with temperature. The value of  $R_{\min}$  at room temperature was found to be of the order of  $10^{-9}$  m. Also,  $R_{\min}$  was found to be  $\sim 10^{-3}$  times smaller in comparison to the grain size of BSN.

## Conclusion

Polycrystalline  $\text{Ba}(\text{Sb}_{1/2}\text{Nb}_{1/2})\text{O}_3$  prepared using a high-temperature solid-state reaction technique was found to have a perovskite-type monoclinic structure. Dielectric study revealed the frequency-dependent dielectric anomaly. Impedance analyses indicated the presence of grain and grain boundary effect in BSN. Sample showed dielectric relaxation, which is found to be of non-Debye-type and the relaxation frequency shifted to higher side with the increase of temperature. The ac conductivity study showed the NTCR character of BSN. The ac conductivity is found to obey the universal power law, and the CBH model is found to successfully explain the mechanism of charge transport in BSN. Further, the frequency dependent ac conductivity at different temperatures indicated that the conduction process is thermally activated process. These results are well supported by density of states at Fermi level and scaled parameters data. The value of minimum hopping length was found to be  $\sim 10^{-3}$  times smaller in comparison to the grain size of BSN.

**Acknowledgements** This study was supported by Defense Research and Development Organization, New Delhi under Grant No. ERIP/ER/0605044/M/01/928.

## References

1. Reaney IM, Petzelt J, Voitsekhovskii VV, Chu F, Setter N (1994) *J Appl Phys* 76:2086
2. Saha S, Sinha TP (2002) *J Phys Condens Matter* 14:249
3. Raevski IP, Prosandeev SA, Bogatin AS, Malitskya MA, Jastrabik L (2003) *J Appl Phys* 93:4130
4. Chung C-Y, Chang Y-H, Chen G-J (2004) *J Appl Phys* 96:6624
5. Wang Z, Chen XM, Ni L, Liu XQ (2007) *Appl Phys Lett* 90:022904
6. Bhagat S, Prasad K (2010) *Phys Status Solidi A* 207:1232
7. Dutta A, Sinha TP (2006) *J Phys Chem Solids* 67:1484
8. Prasad K, Chandra KP, Bhagat S, Choudhary SN, Kulkarni AR (2010) *J Am Ceram Soc* 93:190
9. Prasad K, Bhagat S, Amarnath K, Choudhary SN, Yadav KL (2009) *Phys Status Solidi A* 206:316
10. Prasad K, Bhagat S, Amarnath K, Choudhary SN, Yadav KL (2010) *Mater Sci Pol* 28:317
11. Jones FG, Randall CA, Jang SJ, Shrout TR (1990) *Ferroelectr Lett* 12:55
12. Raibagkar LJ, Bajaj SB (1998) *Solid State Ion* 108:105
13. Prasad K, Bhagat S, Priyanka, Amarnath K, Chandra KP, Kulkarni AR (2010) *Phys B Condens Matter* 405:3564
14. Prasad K, Amar Nath K, Bhagat S, Priyanka, Chandra KP, Kulkarni AR (2010) *Adv Appl Ceram* 109:225

15. Jung W-H, Lee J-H, Sohn J-H, Nam H-D, Cho S-H (2002) Mater Lett 56:334
16. Prasad K, Kumari K, Lily, Chandra KP, Yadav KL, Sen S (2007) Adv Appl Ceram 106:241
17. Prasad K, Lily, Kumari K, Chandra KP, Yadav KL, Sen S (2007) Appl Phys A 88:377
18. Roisnel J, Rodriguez-Carvajal J (2000) Winplotr; Laboratoire Léon Brillouin (CEA-CNRS) Centre d'Etudes de Saclay: Gif sur Yvette Cedex, France
19. Rodriguez-Carvajal J, FullProf (2000) A Rietveld Refinement and Pattern Matching Analysis Program (Version: April 2008), Laboratoire Léon Brillouin (CEA-CNRS), France
20. Sharma GD, Roy M, Roy MS (2003) Mater Sci Eng B 104:15
21. Mollah S, Som KK, Bose K, Chaudri BK (1993) J Appl Phys 74:931
22. Salam R (1990) Phys Status Solidi A 117:535
23. McCusker LB, Von Dreele RB, Cox DE, Louër D, Scardi P (1999) J Appl Crystallogr 32:36
24. Macdonald JR (ed) (1987) Impedance spectroscopy emphasizing solid materials and systems. Wiley, New York
25. Boukamp BA (2004) Solid State Ion 169:65
26. Barsoukov E, Macdonald JR (2005) Impedance spectroscopy theory, experiment and applications, 2nd edn. Wiley-Interscience, Wiley, New Jersey
27. Prasad K, Suman CK, Choudhary RNP (2006) Adv Appl Ceram 105:258